Patterned Two-Photon Photoactivation Illuminates Spatial Reorganization in Live Cells

Adam W. Smith,[†,‡] Alexander A. Smoligovets,[§] and Jay T. Groves*,[†,‡]

[†]Howard Hughes Medical Institute, Department of Chemistry, University of California, Berkeley, California 94720, United States

[‡]Physical Biosciences and Materials Sciences Divisions, Lawrence Berkeley National Laboratory, Berkeley, California 94720, United States

[§]Department of Molecular and Cell Biology, University of California, Berkeley, California 94720, United States

Ⓢ Supporting Information

ABSTRACT: Photoactivatable fluorescent proteins offer the possibility to optically tag and track the location of molecules in their bright state with high spatial and temporal resolution. Several reports of patterned photoactivation have emerged since the development of a photoactivatable variant of the green fluorescent protein (PaGFP) and the demonstration of two-photon activation of PaGFP. To date, however, there have been few methods developed to quantify the spatial reorganization of the photoactivated population. Here we report on the use of singular

value decomposition (SVD) to track the time-dependent distribution of fluorophores after photoactivation. The method was used to describe live-cell actin cytoskeleton behavior in primary murine T-cells, in which a dynamic cytoskeleton is responsible for the reorganization of membrane proteins in response to antigen peptide recognition. The method was also used to observe immortalized simian kidney (Cos-7) cells, in which the cytoskeleton is more stable. Both cell types were transfected with PaGFP fused to the F-actin binding domain of utrophin (UtrCH). Photoactivation patterns were written in the samples with a pair of galvanometric scanning mirrors in circular patterns that were analyzed by transforming the images into a time series of radial distribution profiles. The time-evolution of the profiles was well-described by the first two SVD component states. For T-cells, we find that actin filaments are highly mobile. Inward transport from the photoactivation region was observed and occurred on a 1−2 s time scale, which is consistent with retrograde cycling. For Cos-7 cells, we find that the actin is relatively stationary and does not undergo significant centripetal flow as expected for a resting fibroblast. The combination of patterned photoactivation and SVD analysis offers a unique way to measure spatial redistribution dynamics within live cells.
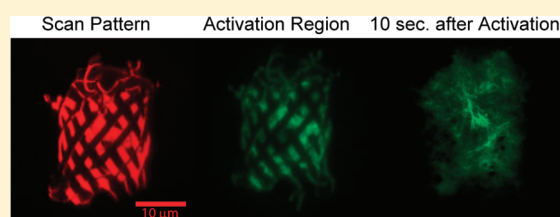
■ INTRODUCTION

Molecular movements in cells do not conform to simple diffusion laws. Within the cell, molecules are synthesized, trafficked, and degraded at high turnover rates. In addition, high molecular densities lead to crowding effects that hinder protein diffusion and create a need for actively driven transport mechanisms. Because trafficking of materials and signals within cells is actively regulated, following their dynamics requires a detailed description of spatial distributions over time. We report a method to track a spatially defined population of molecules as it redistributes within the cell. A matrix decomposition algorithm is used to analyze a series of time-lapse images that are taken after photoactivating a user-defined region of the cell. With this method we describe the time-evolution of patterned distributions of actin within the dense cytoskeletal network of live cells.

Recently developed photoactivatable fluorescent proteins offer the possibility to optically tag and track the location of molecules in their bright state with high spatial and temporal resolution.[1,2] With two-photon photoactivation it is possible to activate spatial distributions of these molecules within volumes limited to hundreds of nanometers in the lateral dimension and close to one micrometer in the axial dimension. Two-photon photoactivation allows for

smaller photoactivation patterns in the axial and lateral dimensions compared to one-photon photoactivation because two-photon absorption depends on the square of the input power. Several studies using two-photon patterned photoactivation have been produced since the development of a photoactivatable variant of the green fluorescent protein (PaGFP) and the demonstration of two-photon activation of PaGFP.[3,4] For example, tissue-level protein migration has been observed by photoactivating a pool of PaGFP in targeted cells.[5,6] In single cells, small regions have been photoactivated to follow nucleocytoplasmic transport[7,8] and chromatin mobility within nuclear compartments.[9] The dynamics of the photoactivated pool of fluorophores are typically analyzed using intensity variations away from the photoactivation region. This is similar to the analysis of photobleaching experiments, but instead of monitoring fluorescence recovery after photobleaching (FRAP), the experiments monitor fluorescence migration after

photoactivation. While analyzing simple intensity variations may be useful for following transport in and out of organelles and from cell to cell, it is not ideal for mapping spatial distributions for which the directionality and flow rates may not be homogeneous across the cell. Here we report on the use of singular value decomposition (SVD) to track the time-dependent distribution of fluorophores after photoactivation. SVD allows for a quantitative description of spatial reorganization without reducing the data to a raw intensity decay and without the need to fit the spatial distribution to a predetermined functional form.

SVD is a matrix algebra operation that is used to treat multivariate data[10−12] by decomposing a data matrix into basis states and weighting coefficients. For a time-dependent set of data, each measurement in time can be reconstructed as a linear combination of the basis states with the corresponding set of time-dependent coefficients. The advantage of SVD is that the weighting coefficients can be used to find so-called high ranking basis states that make the largest contributions to the data set. The high ranking basis states can then be used to identify the dominant changes to the data over time. In this way, SVD functions analogously to a Fourier analysis in that it can be used to remove low-frequency noise from the data. Furthermore, the time-dependent weighting coefficients for the high-ranking basis states can be used to assign rates to the processes represented by those basis states. In our results below, the first and second SVD basis states dominate the time-dependent data set, accounting for over 99% of the intensity. The first component state is highly similar to the time average of the original data, while the profile of the second component state resembles the difference between the data at the first time point and a later time point. The rates of change to the amplitude of the two components are used to describe the time-dependent distribution of a photoactivated ensemble of molecules.

In this work we apply the above methodology to study the actin cytoskeleton of living cells. The dynamics of the actin network are a complex interplay of polymerization and depolymerization rates in feedback with other cellular functions. Cytoskeleton dynamics play an important role in cell function and are sensitive to the biological state of the cell. For this study, cells were transfected with PaGFP fused to the F-actin binding calponin homology domain of utrophin (UtrCH). Photoactivation patterns were written in each sample with a pair of galvanometric scanning mirrors that position the laser focus with accuracy approaching the diffraction limit at the image plane and pixel dwell times as fast as 100μs. Photoactivation was localized to the cortex of the cell near the substrate, and photoactivated proteins were tracked using time-lapse total internal reflection fluorescence (TIRF) microscopy. Several mechanisms redistribute the bright fluorophores throughout the cell including diffusion of unbound fluorophores, fragmentation and regeneration of the cytoskeleton, and migration of the polymer network. These multiple mechanisms create the need to use SVD to characterize actin dynamics. For Cos-7 cells we find that the photoactivated fluorophores redistribute isotropically around the pattern region. This process occurs on a 3.8 s time scale indicating a relatively stable network with no net transport as expected for large adherent cells. For antigen-activated T-cells, we find that the actin filaments are highly mobile. Radial transport from the photoactivation region to the center of the cell occurs at a 1.7 s time scale, which is consistent with retrograde cycling.[13,14] The combination of patterned photoactivation and SVD analysis offers a unique way to measure spatial redistribution dynamics within live cells.

■ EXPERIMENTAL METHODS

Microscope. Photoactivation experiments were performed on an inverted microscope (Nikon Eclipse Ti; Technical Instruments, Burlingame, CA) with a custom-built laser scanning attachment. Photoactivation light was produced by an 80 MHz, 100 fs pulsed Titanium:Sapphire laser (Mai Tai HP; Newport Corp, Mountain View, CA) operating at a typical center wavelength of 775 nm. Laser power at the sample was controlled with an electro-optic modulator (350-80LA; Conoptics Inc., Danbury, CT) and was set to between 5 and 20 mW at the sample. An optical breadboard platform was built to access the infinity space of the microscope below the objective. The photoactivation laser was positioned using a pair of galvanometric scanning mirrors (6215H-M40B; Cambridge Technology Inc., Cambridge, MA) that directed the light through a scan lens (Zeiss EC Plan-Neofluar 2.5x; Edmund Optics Inc., Barrington, NJ) and tube lens (130 mm tube lens; Edmund Optics Inc., Barrington, NJ) positioned as described by Tsai et al.[15] A dichroic beamsplitter (FF670-SDi01-25 × 36; Semrock Inc., Rochester, NY) reflected the light through the objective (Nikon 1.49 N.A. TIRF; Technical Instruments, Burlingame, CA) and allowed >95% transmission from 450 to 690 nm. Exposure times were set in the image collection software (MetaMorph 7.5; Molecular Devices Inc., Downingtown, PA), which drives an external shutter (Uniblitz LS6; Vincent Associates, Rochester, NY). Laser light to the camera was filtered with a short wave pass filter (FF01-680/SP-25; Semrock Inc., Rochester, NY). Because of the intensity requirements for two-photon processes, photoactivation was axially confined to approximately $1−2 \mu$m at the cortical interface between the cell and the substrate.[16]

TIRF microscopy was done using a fiber-coupled Nikon TIRF illuminator (Technical Instruments, Burlingame, CA) with a custom-built laser source. The 643 nm (RCL-050-640; Crystalaser, Reno, NV), 561 nm (GCL-100-561; Crystalaser, Reno, NV), and 488 nm (Sapphire HP; Coherent Inc., Santa Clara, CA) lasers were launched into a single mode fiber that was connected to the TIRF illuminator. Excitation powers at the sample were on the order of 1 kW/cm^2. Images were acquired with an EM-CCD (iXon 597DU; Andor Inc., South Windsor, CT). Bandpass emission filters for 488, 561, and 643 nm TIRF images are HQ515/30, ET630/75, and HQ700/75 (Chroma Technology Corp., Bellows Falls, VT), respectively.

DNA Constructs. Plasmids containing photoactivatable green fluorescent protein or monomeric red fluorescent protein (mRFP) attached to the calponin homology domain of utrophin (PaGFP-UtrCH or mRFP-UtrCH, respectively) were a gift of William Bement, University of Wisconsin, Madison, WI.[17] A retroviral vector for Phoenix cell transfection (discussed below) and subsequent T-cell transduction was generated by amplifying the PaGFP-UtrCH coding sequence using polymerase chain reaction (PCR) and the primers 5′-AGGATCCTCGA-GATGGTGAGCAAGGGCGAGGAGCTGTTCACC-3′ and 5′-AGCTTGGCGGCCGCTTAGTCTATGGTGACTTGCT-GAGGTAGCACCTCAAACAAAGATG-3′ and subcloning the resulting fragment into the XhoI and NotI sites of a murine stem cell virus−internal ribosome entry site−puromycin N-acetyl transferase plasmid.

Phoenix Cell Culture, Transfection, and Retrovirion Production. Phoenix cells, an HEK 293T-based retroviral packaging cell line,[18] were grown in Dulbecco's modification of Eagle's medium (DMEM) supplemented with 10% fetal bovine serum

(Atlanta Biologicals Inc., Lawrenceville, GA), 1 mM sodium pyruvate, 2 mM L-glutamine, 100 U/mL of penicillin, and 100 μg/mL streptomycin. On day 1 of the transduction protocol discussed below, Phoenix cells at a confluency of approximately 70% were cotransfected with the target retroviral plasmid and the packaging plasmid pCL-Eco (Imgenex Inc., San Diego, CA) using the calcium phosphate method. At 6 h after transfection, the Phoenix medium was exchanged, and at 24 h (day 2), it was replaced with T-cell medium (RVC, as previously described[19]). The medium containing retrovirions was collected at 48 h (day 3), when it was replaced with fresh RVC, and at 72 h (day 4).

T-Cell Culture and Transduction. AND CD4+ T-cell blasts were cultured from the lymph nodes and spleens of first generation AND $\times$ B10.BR mice on day 1 of the T-cell transduction protocol in accordance with Lawrence Berkeley National Laboratory Animal Welfare and Research Committee-approved protocol 17702. The cells were stimulated with 2 μM moth cytochrome c (amino acids 88−103) peptide immediately after harvest. At 24 h after harvest (day 2), 50 U/mL mouse recombinant IL-2 (Roche Applied Science Inc., Indianapolis, IN) was added to the T-cell medium. At 48 h (day 3), the T-cells were pelleted and resuspended in Phoenix cell-derived retroviral supernatant filtered through a 0.45 μm PES syringe filter and supplemented with 50 U/mL IL-2 and 4 μg/mL polybrene. They were then centrifuged at 25 °C and 1328g for 1 h and returned to the incubator. At 72 h (day 4), the T-cells were again pelleted, resuspended in filtered and IL-2/polybrene-supplemented retroviral supernatant, centrifuged, and returned to the incubator. At 78 h (day 4), they were pelleted and resuspended in fresh RVC supplemented with 50 U/mL IL-2 and 0.5 μg/mL puromycin. At 120 h (day 6), they were pelleted and resuspended in fresh RVC supplemented with 50 U/mL IL-2. The cells were then used in experiments 168 h after harvest (day 8).

T-Cell Imaging: Preparation of Substrates, Buffers, and Cells. Glass coverslips were etched for 2 to 5 min in piranha etch solution (3:1 H_2SO_4/H_2O_2) and were used in the assembly of FCS2 Closed Chamber Systems (flow cells; Biptechs Inc., Butler, PA), which were prefilled with Tris-buffered saline (19.98 mM Tris, 136 mM NaCl, pH 7.4; Mediatech Inc., Herndon, VA). Solutions of small unilamellar lipid vesicles (0.5−2.0 mg/mL) were prepared by the sonication or extrusion of evaporated mixtures of 2 mol % Ni^{2+}-DOGS/98 mol % DOPC (Avanti Polar Lipids Inc., Alabaster, AL). The lipid solutions were mixed 1:1 with Tris-buffered saline, injected into the flow cells, and incubated at room temperature for approximately 30 min. The flow cell chambers were then rinsed with Tris-buffered saline, incubated with 100 mM NiCl$_2$ for 5 min, rinsed once with Tris-buffered saline, and then rinsed again with an imaging buffer composed of 1 mM $CaCl_2$, 2 mM $MgCl_2$, 20 mM HEPES, 137 mM NaCl, 5 mM KCl, 0.7 mM Na_2HPO_4, 6 mM D-glucose, and 1% fetal bovine serum (HyClone Inc., Logan, UT), pH 7.3 $\pm$ 0.1. Finally, the flow cells were filled with a solution of moth cytochrome c-loaded hexahistidine-tagged MHC protein and 30 nM decahistidine-tagged ICAM-1 protein in imaging buffer,[20,21] incubated at room temperature for 35 min, and then rinsed with imaging buffer and allowed to equilibrate for a further 35 min. During the final incubation, the flow cells were brought to 37 °C.

T-cells at 168 h after harvest (day 8) were pelleted, resuspended in a solution of 5 μL Alexa Fluor 647 (Invitrogen Inc., Carlsbad, CA)-conjugated H57 anti-TCR antibody fragment (F_{ab}): 100 μL imaging buffer and incubated on ice for 20 min.

They were then rinsed with imaging buffer, pelleted, resuspended in imaging buffer, and injected into flow cell chambers upon the completion of the flow cell equilibration. Throughout the T-cell imaging process, the flow cell chambers were kept at 37 °C, and all images were acquired within 90 min after the cells were injected into the flow cell chambers.

Cos-7 Cell Culture, Transfection, and Preparation for Imaging. Cos-7 cells were grown in DMEM supplemented with 10% fetal bovine serum (Atlanta Biologicals Inc., Lawrenceville, GA), 1 mM sodium pyruvate, and 2 mM L-glutamine. They were transfected using Lipofectamine 2000 and the associated protocols (Invitrogen Inc., Carlsbad, CA) 48 h after being seeded on 6-well plates at 2.5×10^5 cells per well in 2 mL of medium. The Cos-7 medium was exchanged 24 h after transfection, and the cells were imaged 48 h after transfection.

Prior to imaging, piranha-etched glass coverslips were coated in 0.01% (w/v) poly-L-lysine, dried, and used in the assembly of open-top cover glass imaging chambers. Transfected Cos-7 cells were rinsed once with phosphate-buffered saline and then treated with 0.5% phenol red-free trypsin-EDTA for 5 min. Following trypsinization, the cells were rinsed with phenol red-free DMEM, pelleted, resuspended in phenol red-free DMEM, and added to the cover glass chambers. They were then incubated at 37 °C/5% CO_2 for 30 min prior to imaging. For imaging the photoactivation patterns used in SVD analysis, cover glass chambers were kept at 37 °C throughout the measurement, while more complex images of custom photoactivation patterns were acquired with the live cells at room temperature.

For fixed-cell experiments, Cos-7 cells were added to the cover glass chambers and incubated at 37 °C/5% CO_2 as described above. After 30 min, cells were rinsed with phosphate-buffered saline, fixed with 10% formalin (4% formaldehyde; Sigma-Aldrich Corp, St. Louis, MO) for 20 min, and rinsed twice with phosphate-buffered saline. Images were acquired with the fixed cells prewarmed to 37 °C.

Optical Patterning. Photoactivation patterns were generated using two different scanning modes. In the first, the mirrors were scanned continuously using the output of a waveform generator. In Figure 1b, for example, the drive voltage to each mirror was scanned from −60 to 60 mV using a 1 kHz sine wave with a 90° phase between the mirrors. The total photoactivation time was controlled with an external laser shutter timed with the camera acquisition. Exposure times varied across experiments but ranged between 0.1 and 1.5 s so that the pattern was traced on the sample 100 to 1500 times. To create the line shown in Figure 1a, only one mirror was scanned using a 1 kHz ramp waveform at ±70 mV.

In the second scanning mode, patterns were written using customized software integrated with the MPScope two-photon imaging package.[22] The software defined a field of view by a minimum and maximum scanning voltage, which was divided into a 512 $\times$ 512 grid of pixel positions. The program allowed access to arbitrary pixels at definable dwell times and was limited only by the small angle response time of the galvanometer mirror set ($\sim$100 μs). The pattern shown in Figure 1h was programmed as a sequential set of pixel positions (285 total pixel positions) with 1 ms pixel dwell times. Total photoactivation exposure times were set to 3−5 times the pattern rate. When the custom software was used in this modality, it was possible to build arbitrary scan patterns as shown in Figure S1, which depicts a cartoon drawing of the green fluorescent protein downloaded from nobelprize.org.[23] The image was made by creating a binary
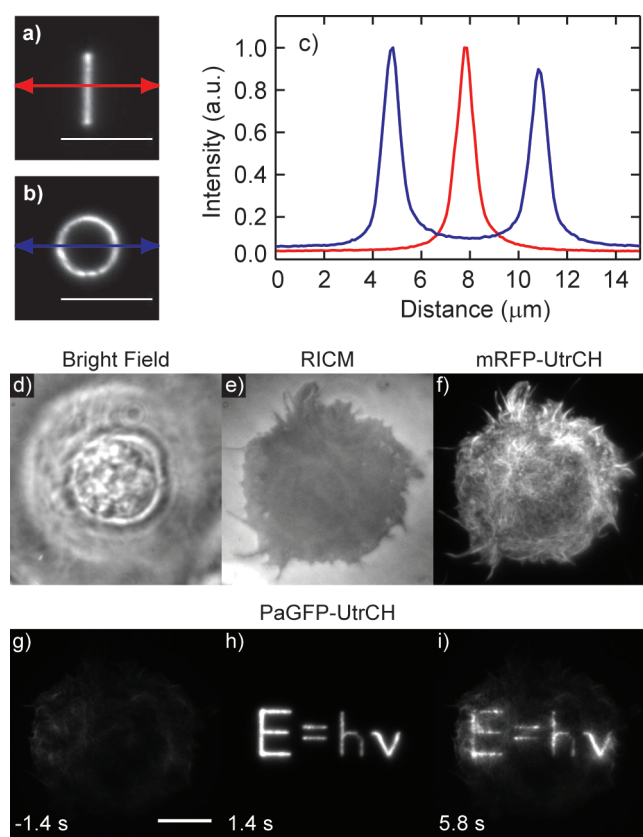
Figure 1. (a,b) Simple patterns used in live cell experiments. Images are from two-photon excitation during the photoactivation frame. (a) Line scan 6.5 μm long. (b) Circle scan 3.0 μm radius. (c) Image slices shown for circle and line scans. The full width at half of peak maximum is $\approx$0.9 μm. (d−i) Images of a live Cos-7 cell showing fluorescence before and after exposure of the custom photoactivation pattern consisting of 285 pixels scanned at a rate of 1 ms/pixel for 1 s duration. This cell was also transfected with mRFP-UtrCH to highlight the underlying cytoskeleton in the absence of photoactivation. Frames (d-f) show bright field (d), RICM (e), and mRFP-UtrCH 561 nm TIRF (f) images. Bottom row shows 488 nm TIRF images at −1.4 (g), 1.4 (h), and 5.8 s (i) after photoactivation. All image scale bars represent 10 μm.

mask from the original JPG file that defined the set of 14855 pixels to be exposed. With 0.1 ms pixel dwell times, the total pattern time was 1.45 s, so that the pattern was traced 5 times during the exposure for Figure S1a. In both of the patterning modalities described above, the lateral photoactivation resolution was consistent with previous work.[16] The line scans in Figure 1c showed a full width at half-maximum of 900 nm.

RESULTS AND DISCUSSION

Patterned Photoactivation in Cells. To demonstrate the feasibility of visualizing a discrete ensemble of photoactivated proteins within a live cell, we chose to observe the actin cytoskeleton, a highly organized yet dynamic protein network ubiquitous among eukaryotes. There are a number of probes available for visualizing the actin cytoskeleton in live cells, which encompass three broad categories, each with distinct advantages and disadvantages: fluorescently labeled phalloidin, fluorescent G-actin, and labeled actin binding proteins or domains (ABPs).[17,24] For studying cytoskeletal dynamics, phalloidin, a cell-impermeant F-actin binding small molecule, must be microinjected into live cells, which

is laborious and extremely low-throughput.[24] Fluorescent protein (FP)-conjugated G-actin and ABPs can conveniently be genetically encoded to enable higher-throughput data acquisition, but both can also interfere with the cytoskeletal dynamics they are intended to probe. FP-actin fails to rescue actin knockouts in yeast,[25] and *Dictyostelium discoideum* cells transfected with FP-actin show significantly altered cell morphology,[26] indicating that the fluorescent protein adduct has some effect on wild-type actin function. Indeed, there is evidence that cytoskeletal dynamics measured by FP-actin labeling may not correspond to endogenous values.[24] These defects are typically avoided by the use of FP-ABPs; however, actin binding domains can instead compete with similar domains in endogenous proteins.[24,27] While the overall cell phenotype typically remains much closer to wild-type with FP-ABPs than with FP-actin, one further consideration in their use is that F-actin binding domains may unbind from cytoskeletal filaments, making them potentially more diffusive than FP-actin. Both FP-ABPs and FP-actin can also have separate and distinct incorporation biases for certain cellular actin pools.[17,25,28] To minimize disruption of endogenous actin filament polymerization and depolymerization dynamics, we chose to label the cytoskeleton with a fluorescently labeled probe composed of the calponin homology domain of the actin binding protein utrophin (UtrCH).[17] This probe robustly labels F-actin in both cellular systems we employed and remains strongly bound to filaments on the time scale of our experiments.

We photopatterned the actin cytoskeleton labeled with PaGFP-UtrCH in live immortalized simian kidney (Cos-7) cells that were seeded onto poly-L-lysine-coated substrates. For each cell, bright field, reflection interference contrast microscopy (RICM), and TIRF images (488 and 561 nm excitation) were acquired before photoactivation. The cell was then exposed to the scanning photoactivation laser, which traced a pattern of arbitrary complexity on the cytoskeleton. Following the photoactivation, a sequence of 488 nm TIRF images was taken at 2 frames per second.

A series of images following the preceding protocol is shown in Figure 1d−i. Cos-7 cells are relatively large, adherent cells with extended plasma membrane regions that generate little contrast in the bright field image (Figure 1d). The RICM image (Figure 1e) shows the outline of the cell, and the even intensity shows that it adheres well to the poly-L-lysine coated substrate. The cells were also cotransfected with mRFP-UtrCH so that the actin filament network could be imaged independent of photoactivation (Figure 1f). Before activation, the 488 nm TIRF image shows very little intensity (Figure 1g). Figure 1h shows the photoactivated population 1.4 s after the beginning of the exposure to the scanning laser pattern. At 5.8 s (Figure 1i), the pattern is blurred due to a combination of bleaching and diffusion/transport of PaGFP-UtrCH.

Spatial Dynamics with Singular Value Decomposition. The dynamics of the actin network are a complex interplay of polymerization and depolymerization rates in feedback with other cellular functions. Arp2/3 and WASP proteins, for example, nucleate filaments and control branching, which help define the size and density of actin filaments.[29] The function of actin cofactors is highly regulated within the cell, and it is therefore essential that the dynamics of the actin network be studied in situ. One limiting factor in imaging the actin network is its high density, which hinders observation of molecular turnover during polymerization and depolymerization. Speckle imaging[30] and single molecule tracking[31] are well-suited for molecular turnover assays because the fate of individual monomer units can be
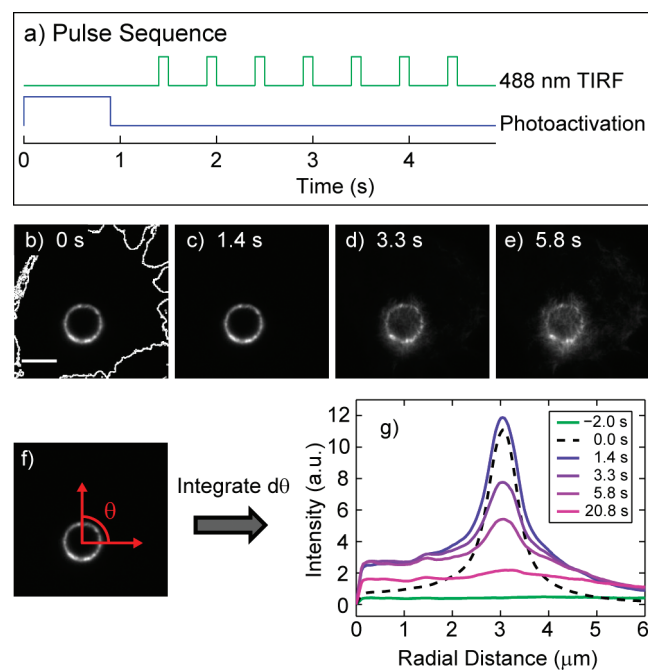
Figure 2. (a) Diagram of the image collection sequence shows the 900 ms photoactivation pulse followed by a 2 Hz pulse train of 100 ms exposures of 488 nm TIRF. (b–e) Selected images from time-lapse imaging of a live Cos-7 cell. At $t = 0$ s (b), the scanned circular pattern (3 μm radius) is exposed to the cell outlined in white. Subsequent 488 nm TIRF images are collected at the specified times. Image intensities are rescaled for each frame to highlight topology. (f) Each image is centered to the activation ring, transformed into polar coordinates, and integrated with respect to the angle. (g) Time series of integrated radial distributions used in the SVD analysis. Scale bar in (b) represents 5 μm.

measured over time. Both methods, however, are limited in application and in the type of information one can obtain. Speckle imaging requires a specific density of fluorophore that is difficult to control experimentally, particularly in primary cell lines. More importantly, speckle microscopy requires an algorithm for particle identification and tracking that is prone to interpretive error.[32] Single molecule methods in live cells have been difficult in the past because the diffraction limit of optical microscopes limits the allowable density of fluorophores and thus undersamples the cortical actin meshwork. Photoactivatable probes have revived this method because small populations can be stochastically activated, localized, and tracked.[31] The weakness of this approach is that dynamic information is uncorrelated over the total acquisition time and that the duration of individual tracks is fundamentally limited by fluorophore bleaching.

Patterned photoactivation offers a complementary method to track small, spatially defined populations of molecules for longer times than other methods. The bright ensemble samples the pattern area, and intensity shifts out of the activation region can be directly related to molecular transport. To make the best use of patterned photoactivation time-lapse images, a quantitative method is needed to describe the time-evolution of the spatial distributions. In the few patterned photoactivation studies to date, the data have typically been quantified by measuring intensity decays/increases in user-defined regions of interest.[7,8] While simple and functional, this approach is prone to bias and does not make full use of the information available in the data. To overcome these limitations, we used SVD to decompose the time-dependent spatial distribution

into components ranked by their contribution to the time-evolution of the data set. In this way, the spatial and temporal information was conserved and could be used to better characterize the dynamics of the system.

SVD is a commonly used algorithm that has found applications ranging from time-resolved spectroscopy to DNA microarray analysis.[10−12,33] In one typical application, SVD is used to analyze time-dependent spectroscopy data following a perturbation.[11,12,34] SVD simplifies the analysis of time-evolving spectra that are simultaneously undergoing peak shifts, line broadening, and frequency-dependent intensity changes. In a similar way, it is difficult to characterize time-lapse images of photopatterned regions that are shaped by multiple effects like bleaching, lateral diffusion, axial diffusion out of the observation volume, and directed transport or flow. In the present work SVD is used to analyze the time-dependent, postphotoactivation images, where the pattern-activated ensemble is simultaneously shifting and decaying without a well-defined final state.

SVD analysis was first applied to PaGFP-UtrCH photoactivated in Cos-7 cells, which are nonmotile and in which the actin cytoskeleton is expected to be relatively stable based on an observed lack of filament turnover and actin flow. A 3 μm radius ring was photoactivated near the center of the cell (Figure 2b) using the pattern technique introduced in Figure 1b. Images are represented by the variable: $\mathbf{I}(x,y,t)$. The data are first reduced to two dimensions by taking advantage of the radial symmetry of the photoactivation pattern. This is motivated by the centro-symmetric retrograde flow in T-cells that will be discussed in the following section. The center of the activation annulus is defined as the origin, and the spatial x and y positions are transformed into polar coordinates. The image matrix is then integrated over the azimuthal angle, so that the traces represent the radial distribution of the fluorophores (see Figure 2f):

$$\mathbf{I}(x, y, t) \rightarrow \mathbf{I}(r, \theta, t); \ \mathbf{D}(r, t) = \int \mathbf{I}(r, \theta, t)\, \mathrm{d}\theta$$

Several time points from the resultant data matrix, $\mathbf{D}(r,t)$, are shown in Figure 2g.

In the following implementation of SVD, $\mathbf{D}(r,t)$ is an $m \times n$ matrix, where the m dimension is the radial profile of the fluorescence intensity, r and n, is the time dimension, t. SVD decomposes $\mathbf{D}$ so that

$$\mathbf{D} = \mathbf{U}\mathbf{S}\mathbf{V}^{\mathbf{T}}$$

Where $\mathbf{U}$ is an $m \times n$ matrix with n orthonormal basis states, $\mathbf{V}^{\mathbf{T}}$ is an $n \times n$ matrix with each row representing the time-evolution of the corresponding basis state, and $\mathbf{S}$ is an $n \times n$ diagonal matrix where elements $s_{i,i}$ are the singular values, or weighting factors.

The first three component basis states from the data in Figure 2 are shown in Figure 3c. The singular values $s_{1,1}$, $s_{2,2}$, and $s_{3,3}$ are 2.2×10^7, 3.9×10^6, and 6.8×10^5, respectively. The ratio of these values falls into a range where the first and second basis states represent the majority of the changes over time but cannot be rigorously separated from the other data. In this regime, the SVD analysis is analogous to a Fourier filter that isolates and ranks the dominant components of the time-dependent spatial distribution. For the time-lapse images shown in this report, the first component basis state (Figure 3c, blue) is nearly identical to the time average of $\mathbf{D}(r,t)$ (shown in Figure S2), and its weighting factor over time is dependent on total fluorophore intensity. The decay of the first component is shown in Figure 3d
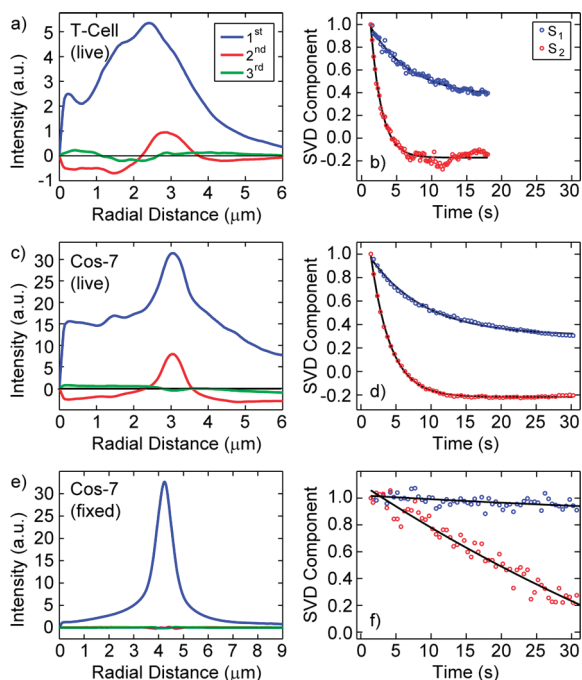
Figure 3. Summary of SVD results for three representative cells. Top row: Live T-cell. Panel (a) shows the first three SVD component states from the data in Figure 4 scaled by their value at $t = 1.3$ s. (b) The decays of the SVD components over time (normalized to $t = 1.3$ s) are fit to a single exponential function ($y = c + A \cdot e^{-t/\tau}$) with $\tau_{first} = 5.3$ s and $\tau_{second} = 1.6$ s. Middle row: Live Cos-7 cell. Panel (c) shows the first three SVD component states from the data in Figure 2 scaled by their value at $t = 1.4$ s. (d) The decays of the normalized SVD components over time are fit to the single exponential function above with $\tau_{first} = 7.8$ s and $\tau_{second} = 2.8$ s. Bottom row: Fixed Cos-7 cell. Panel (e) shows the first three SVD component states for data collected from fixed Cos-7 cells described in the text. (f) The decays of the normalized SVD components over time (up to 90 s) are fit to the single exponential function above with $\tau_{first} = 89$ s and $\tau_{second} = 87$ s. Note that the fitted time constants are at the end of the data series and therefore can only represent a lower bound to the time decay.

(blue) and is interpreted to represent photobleaching and axial transport of the fluorophores out of the TIRF excitation region. The second component basis state (Figure 3c, red) is very similar to the difference between the radial distributions over time (i.e., $\mathbf{D}(r, t = 0) - \mathbf{D}(r, t = 5$ s); see Figure S2). It is interpreted as the shift in the radial distribution of the fluorophores, so that the decay of the second component (Figure 3d, red) over time is assigned to lateral transport.

The first SVD basis state of the data above shows an even intensity inside the activation ring and slowly decaying intensity at increasing radial distance. The time decay of the first SVD component (Figure 3d, blue) is well described by a single exponential function with $\tau = 7.8$ s. This is interpreted as the time scale for photobleaching and axial migration of fluorophores out of the TIRF excitation volume. The second SVD basis state shows a maximum at the activation ring radius and two symmetric lobes of opposite sign away from the activation ring. This means that actin transport away from the activation ring has no directional bias toward or away from the center of the ring, as expected for a largely stable cytoskeletal network. The rate of lateral transport is found by fitting the time decay of the second component basis state to a single exponential function with $\tau = 2.8$ s.

To confirm that our interpretation of the SVD analysis was based on actual cytoskeletal dynamics, patterned photoactivation was also done on live and fixed Cos-7 cells under identical imaging conditions. The photoactivation area in this case was a 4 μm radius ring, and the postactivation time-lapse imaging protocol was similar to that shown in Figure 2. The lateral transport dynamics of the live cells, quantified as the decay of the second SVD component, are nearly identical to those in Figure 2 (data not shown), with an average $\tau = 3.8 \pm 0.6$ ($N = 5$). The fixed cells, however, show a dramatic difference in the profile of the first and second component basis states (Figure 3e) and in the time decay of the component coefficients (Figure 3f). The first component basis state ($s_{1,1} = 2.0 \times 10^8$) is 2 orders of magnitude larger than all the other components ($s_{2,2} = 1.8 \times 10^6$) and looks identical to the time average of the images. The first component coefficient does not decay appreciably with time, reflecting the fact that there is very little change in the radial profile or the intensity of the photoactivated fluorophore distribution. This is evidence that photobleaching may not play a dramatic role in the decay of the first component in the live cell data. While it is possible that the photostability of the fluorophores may be different in the two different environments, it is still likely that axial transport out of the TIRF illumination volume plays a major role in the decay of the first component basis state in live cells. The second component state of the fixed cells no longer looks like the difference in the radial distribution over time, and the decay of that component coefficient is very slow (>83 s). This is an expected result of the fixation process, which cross-links fluorophores and hinders their lateral transport. The identical set of experiments was performed on several cells, giving an average $\tau = 58 \pm 33$ ($N = 4$).

Actin Dynamics in Live T-Cells. The actin cytoskeleton of T-cells is more dynamic than that of Cos-7 cells. It must enable T-cells in their native environment to crawl through narrow gaps in epithelial sheets in response to secreted chemokines. Upon T-cell antigen recognition on an antigen-presenting cell, the cytoskeleton adopts a pattern of planar, centrosymmetric retrograde flow characterized by actin polymerization near the cell periphery and net transport of monomers within filaments toward the center of the cell—cell interaction.[35] At the same time, the T-cell surface undergoes a dramatic actin-dependent protein rearrangement to generate an ordered T-cell/antigen-presenting cell interface known as the immunological synapse.[36]

Exactly how the cytoskeleton acts to rearrange the surface proteins is still under debate. The Brownian ratchet model of actin monomer addition to a filament near a fluctuating plasma membrane describes a mechanism by which actin polymerization can generate force.[37,38] When such a filament is able to move relative to the cell cortex, any proteins that are directly or indirectly coupled to it may be pulled by this polymerization-driven retrograde flow.[21] Alternatively, if the cargo protein itself is a site of filament nucleation, it may be pushed by a polymerizing but nonmotile filament.[37] Both mechanisms may also be affected by the presence of myosins, actin binding proteins that can actively move cargo along filaments, slide filaments with respect to each other, or anchor filaments to each other or to the cell substratum.[39] Actin retrograde flow has so far been observed in the immortalized Jurkat T-cell line using fluorescence speckle microscopy,[14,40] and while this method has clearly shown monomer retrograde flow in this system, the characterization of larger-scale filament dynamics remains incomplete due to a lack of methodology to describe them. Furthermore, it is not well-established how Jurkat cell actin dynamics compare to those of primary T-cells.
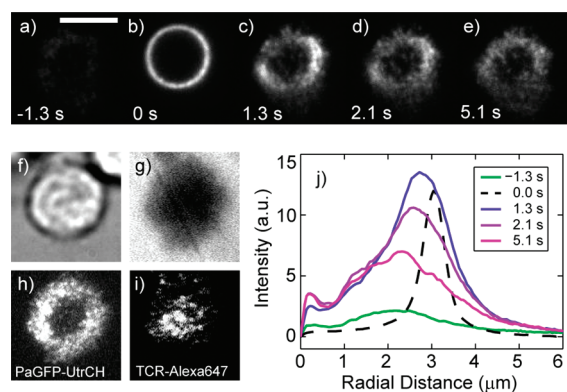
3872

dx.doi.org/10.1021/jp108295s |*J. Phys. Chem. A* 2011, 115, 3867–3875

Figure 4. Photoactivation in live, antigen-activated T-cells. (a–e) Time-lapse images of PaGFP-UtrCH are taken at sample time points before (a), during (b), and after (c–e) photoactivation with the same pattern as in Figure 2. Bright field (f), RICM (g), PaGFP-UtrCH (h), and TCR-Alexa Fluor 647 (i) images are taken before photoactivation. (j) Integrated radial slices at sample time points corresponding to images above. Scale bar in (a) represents 5 μm.

We applied the SVD analysis to primary murine T-cells, which are nonmotile during their triggering, but which, unlike Cos-7 cells, have highly dynamic actin cytoskeletons. T-cells were retrovirally transduced with PaGFP-UtrCH and then presented to a supported lipid bilayer containing agonist peptide-major histocompatibility complex (pMHC) and intercellular adhesion molecules (ICAM-1), which is an established model system that triggers T-cell activation.[36,41] Each set of experiments also included fluorescent images of labeled T-cell receptors (TCR) and ICAM-1 to confirm that the cells under study were forming the canonical protein patterns at the immunological synapse (Figure S3).

Ring photoactivation patterns were used to follow the dynamics of the immunological synapse. First, a 3 μm radius ring was activated near the periphery of the cell, and images postactivation were recorded at 5 Hz frame rates. In Figure 4, several images are shown before, during, and after photoactivation, along with the corresponding radial profiles. The largest redistribution of intensity occurs between photoactivation and the first frame (1.3 s, Figure 4j), where the width of the main peak in the radial distribution is at least twice that of the original activation pattern. This is in contrast to the Cos-7 data, where the radial distribution at t = 1.4 s (Figure 2c) is very similar in width to the original photoactivation ring. We propose that this difference in the magnitude of immediate PaGFP redistribution between T-cells and Cos-7 cells is due to the presence, in T-cells, of highly mobile and potentially segmented actin filaments consistent with those cells' observed dynamic cytoskeletons. However, we cannot exclude the possibility that T-cells may contain a larger population of unbound PaGFP-UtrCH than Cos-7 cells. If this were the case, it would likely be due to a smaller-than-expected F-actin pool in T-cells relative to Cos-7 cells as opposed to relatively higher expression of the probe in the former cell type, since the absolute value of the PaGFP signal was very similar across both cell types.

The radial distribution profiles after 100 ms show a shift toward the center of the cell. This is seen in the peak maxima of the profiles in Figure 4j and in the second SVD component of the radial distribution profile (Figure 3a). The positive peak in second SVD component at the ring radius and the negative intensity in the central region show that intensity is shifting inward with a time constant of 1.6 s. This same measurement was
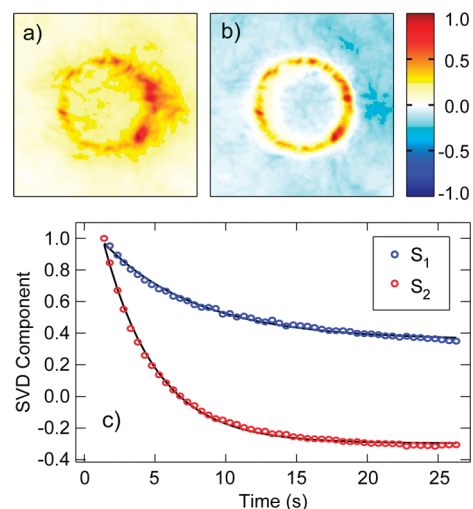

Figure 5. SVD whole-image analysis of the image sequence from Figure 2. Top panels show the first (a) and second (b) component states normalized to their respective maxima. (c) The decay of the image SVD components over time (normalized to t = 1.4 s) are fit to a single exponential function ($y = c + A \cdot e^{-t/\tau}$) with τ_{first} = 6.6 s and τ_{second} = 3.7 s.

made in several cells that give an average time constant of 1.7 ± 0.4 s (N = 17). To test if the time constant for the second SVD component decay is dependent on the frame rate, we repeated the measurement in the same cell at 2 and 5 Hz acquisition frame rates. We found that the fitted time constants of the second SVD component decay at the two acquisition rates were 95% similar.

The shape and time decay of the second SVD component are evidence that F-actin is being transported from the periphery of the cell to the center, consistent with observations of retrograde flow.[13,14,40] Also visible in the images and radial profiles is an actin depletion zone with a radius of about 0.8 μm, which is consistent with previous experiments. A second measurement was performed on the same cell with a smaller activation radius that matched the actin depletion zone (Figure S4). As expected, there was little photoactivation corresponding to a low local actin concentration in that region, but there was additionally very little transport of F-actin out of the center of the immunological synapse. These data were also consistent with actin retrograde flow.

■ CONCLUSIONS

In this work we have shown that patterned two-photon photoactivation and singular value decomposition can be used to track an ensemble of molecules in live cells. Circular activation patterns were analyzed by transforming the time-lapse images into a time series of radial distribution profiles. The time-evolution of the distribution profiles is well-described by the first two SVD component states. In activated T-cells the lateral redistribution is consistent with two types of motion. First, there is a fast spread of intensity out of the activation region that is faster than the lag time between photoactivation and the first image acquisition. This is attributed to highly dynamic filaments and unbound PaGFP-UtrCH. The second motion has a longer time constant as observed in the second component state, and is a measure of dynamic actin filaments migrating to the center of the cell. These results are consistent with a cortical actin network that is mobile and undergoes continual retrograde flow. By contrast, in Cos-7 cells, radial actin distribution

following photoactivation shows no directional bias, as expected for a more stable cytoskeletal network.

When the singular value decomposition method is used, it is possible to identify the dominant components of change in the lateral distribution of fluorophores within a single cell. This makes SVD a useful tool in the processing of image data from patterned photoactivation and patterned photobleaching experiments. One drawback of SVD is that the interpretation of the components and decays is dependent on the pattern. The ring patterns and radial profiles used in this study will not be appropriate for every application. For more general applications, the method can be applied directly to the images themselves without reducing them to a one-dimensional profile. An example of this is shown in Figure 5, which is the two-dimensional SVD of the images taken for Figure 2. Because of computational restrictions, we limit the analysis to a 150 × 150 pixel area. The first and second image components are analogous to those from the radial profile analysis in that the first component basis state represents the average of the image sequence and the second component basis state represents lateral transport. Furthermore, the time decays of the component coefficients match those in Figure 3 very well. This type of analysis could be used to quantify the dynamics of more complex photoactivation patterns in the future.

Fluorescence microscopy is a powerful tool for live cell experiments, but one must negotiate between labeling methods and imaging modalities. At high labeling densities the optical diffraction limit makes fine structures difficult to resolve. At low labeling densities it is possible to localize particles with high resolution, but the image features are susceptible to Nyquist aliasing, and the photophysics of the fluorophore limit the total time of observation. Photoactivatable fluorescent proteins have made it possible to control the effective fluorophore density within cells. With patterned photoactivation, a regime can be accessed between high and low labeling densities in which it is feasible to follow the dynamics of small populations of molecules with a well-defined starting point. By combining a system-motivated activation pattern with a quantitative image analysis tool like SVD, it is possible to make detailed observations of protein spatial dynamics within living cells.

■ ASSOCIATED CONTENT

ⓢ Supporting Information. Additional data are presented, including alternative photoactivation patterns, comparison of the SVD component states to the average and difference profiles, and images showing proper T-cell activation on supported lipid bilayers. This material is available free of charge via the Internet at http://pubs.acs.org.

■ AUTHOR INFORMATION

Corresponding Author
*E-mail: jtgroves@lbl.gov.

■ ACKNOWLEDGMENT

■ REFERENCES

(1) Hell, S. W. *Science* **2007**, *316*, 1153.
(2) Lukyanov, K. A.; Chudakov, D. M.; Lukyanov, S.; Verkhusha, V. V. *Nat. Rev. Mol. Cell Biol.* **2005**, *6*, 885.
(3) Schneider, M.; Barozzi, S.; Testa, I.; Faretta, M.; Diaspro, A. *Biophys. J.* **2005**, *89*, 1346.
(4) Post, J. N.; Lidke, K. A.; Rieger, B.; Arndt-Jovin, D. J. *FEBS Lett.* **2005**, *579*, 325.
(5) Stark, D. A.; Kulesa, P. M. *Dev. Dyn.* **2007**, *236*, 1583.
(6) Murray, M. J.; Saint, R. *Development* **2007**, *134*, 3975.
(7) Martini, J.; Schmied, K.; Palmisano, R.; Toensing, K.; Anselmetti, D.; Merkle, T. *J. Struct. Biol.* **2007**, *158*, 401.
(8) Chen, Y.; Macdonald, P. J.; Skinner, J. P.; Patterson, G. H.; Müller, J. D. *Microsc. Res. Tech.* **2006**, *69*, 220.
(9) Wiesmeijer, K.; Krouwels, I. M.; Tanke, H. J.; Dirks, R. W. *Differentiation* **2008**, *76*, 83.
(10) Wall, M.; Rechtsteiner, A.; Rocha, L. Singular Value Decomposition and Principal Component Analysis. *A Practical Approach to Microarray Data Analysis* **2003**, 91.
(11) Hofrichter, J.; Henry, E. R.; Sommer, J. H.; Deutsch, R.; Ikeda-Saito, M.; Yonetani, T.; Eaton, W. A. *Biochemistry* **1985**, *24*, 2667.
(12) Shrager, R. I.; Hendler, R. W. *Anal. Chem.* **1982**, *54*, 1147.
(13) Lin, C.-H.; Thompson, C. A.; Forscher, P. *Curr. Opin. Neurobiol.* **1994**, *4*, 640.
(14) Kaizuka, Y.; Douglass, A. D.; Varma, R.; Dustin, M. L.; Vale, R. D. *Proc. Natl. Acad. Sci. U.S.A.* **2007**, *104*, 20296.
(15) Tsai, P. S.; Nishimura, N.; Yoder, E. J.; Dolnick, E.; White, G. A.; Kleinfeld, D. Principles, design and construction of a two-photon laser-scanning microscope for in vitro and in vivo brain imaging. In *In Vivo Optical Imaging of Brain Function*; Frostig, R. D., Ed.; CRC Press: Boca Raton, 2002; p 113.
(16) Pantazis, P.; Gonzalez-Gaitan, M. *J. Biomed. Optics* **2007**, *12*, 044004.
(17) Burkel, B. M.; von Dassow, G.; Bement, W. M. *Cell Motil. Cytoskeleton* **2007**, *64*, 822.
(18) Pear, W. S.; Nolan, G. P.; Scott, M. L.; Baltimore, D. *Proc. Natl. Acad. Sci. U.S.A.* **1993**, *90*, 8392.
(19) DeMond, A. L.; Mossman, K. D.; Starr, T.; Dustin, M. L.; Groves, J. T. *Biophys. J.* **2008**, *94*, 3286.
(20) Nye, J. A.; Groves, J. T. *Langmuir* **2008**, *24*, 4145.
(21) Hartman, N. C.; Nye, J. A.; Groves, J. T. *Proc. Natl. Acad. Sci. U.S.A.* **2009**, *106*, 12729.
(22) Nguyen, Q.-T.; Tsai, P. S.; Kleinfeld, D. *J. Neurosci. Methods* **2006**, *156*, 351.
(23) *GFP*, 2008; Vol. *2010*; Nobelprize.org.
(24) Riedl, J.; Crevenna, A. H.; Kessenbrock, K.; Yu, J. H.; Neukirchen, D.; Bista, M.; Bradke, F.; Jenne, D.; Holak, T. A.; Werb, Z.; Sixt, M.; Wedlich-Soldner, R. *Nat. Methods* **2008**, *5*, 605.
(25) Doyle, T.; Botstein, D. *Proc. Natl. Acad. Sci. U.S.A.* **1996**, *93*, 3886.
(26) Aizawa, H.; Sameshima, M.; Yahara, I. *Cell Struct. Funct.* **1997**, *22*, 335.
(27) Hozumi, S.; Maeda, R.; Taniguchi, K.; Kanai, M.; Shirakabe, S.; Sasamura, T.; Spader, P.; Noselli, S. p.; Aigaki, T.; Murakami, R.; Matsuno, K. *Nature* **2006**, *440*, 798.
(28) Wu, J.-Q.; Pollard, T. D. *Science* **2005**, *310*, 310.
(29) Rohatgi, R.; Ma, L.; Miki, H.; Lopez, M.; Kirchhausen, T.; Takenawa, T.; Kirschner, M. W. *Cell* **1999**, *97*, 221.
(30) Waterman-Storer, C. M.; Desai, A.; Chloe Bulinski, J.; Salmon, E. D. *Curr. Biol.* **1998**, *8*, 1227.
(31) Manley, S.; Gillette, J. M.; Patterson, G. H.; Shroff, H.; Hess, H. F.; Betzig, E.; Lippincott-Schwartz, J. *Nat. Methods* **2008**, *5*, 155.
(32) Vallotton, P.; Small, J. V. *J. Cell Sci.* **2009**, *122*, 1955.
(33) Chung, H. S.; Khalil, M.; Tokmakoff, A. *J. Phys. Chem. B* **2004**, *108*, 15332.
(34) Chen, W. G.; Braiman, M. S. *Photochem. Photobiol.* **1991**, *54*, 905.
(35) Burkhardt, J. K.; Carrizosa, E.; Shaffer, M. H. *Annu. Rev. Immunol.* **2008**, *26*, 233.

(36) Grakoui, A.; Bromley, S. K.; Sumen, C.; Davis, M. M.; Shaw, A. S.; Allen, P. M.; Dustin, M. L. *Science* **1999**, *285*, 221.

(37) Theriot, J. A. *Traffic* **2000**, *1*, 19.

(38) Fletcher, D. A.; Geissler, P. L. *Annu. Rev. Phys. Chem.* **2009**, *60*, 469.

(39) Wilson, C. A.; Tsuchida, M. A.; Allen, G. M.; Barnhart, E. L.; Applegate, K. T.; Yam, P. T.; Ji, L.; Keren, K.; Danuser, G.; Theriot, J. A. *Nature* **2010**, *465*, 373.

(40) Yu, C.-H.; Wu, H.-J.; Kaizuka, Y.; Vale, R. D.; Groves, J. T. *PLoS ONE* **2010**, *5*, e11878.

(41) Mossman, K. D.; Campi, G.; Groves, J. T.; Dustin, M. L. *Science* **2005**, *310*, 1191.